

Unveiling the Role of Transition-Metal Ions in the Thermal Degradation of Layered Ni–Co–Mn Cathodes for Lithium Rechargeable Batteries

Sung-Kyun Jung,* Hyungsub Kim, Seok Hyun Song, Seongsu Lee, Jongsoon Kim, and Kisuk Kang*

The need for batteries with high energy density and safety has motivated the development of Ni-rich layered cathodes with high thermal stability, requiring a revisit of the role of the transition-metal ion in the phase transition accompanying the oxygen evolution of highly charged cathodes. Here, the role of the transition-metal ion in $\text{Li}_x\text{Ni}_{0.5}\text{Co}_{0.2}\text{Mn}_{0.3}\text{O}_2$ ($x = 0.5, 0.33$) is revealed in the phase transition and O_2 evolution occurring at high temperatures using combined in situ high-temperature neutron diffraction (ND) and gas analyses. The thermal migration of each transition-metal ion upon heating is directly visualized at different states of charge using Rietveld refinement of ND patterns as well as the maximum entropy method. The oxygen evolution observed for the highly charged state at low temperature is accompanied by M_3O_4 -type spinel ($\text{M} = \text{Ni}, \text{Co}, \text{and Mn}$) phase formation with preferential occupation of Co in the tetrahedral site. $\text{Co}^{3+}/\text{Co}^{2+}$ reduction accompanying the oxygen evolution rather can mitigate and delay the formation of the rock-salt phase. The findings provide insight into the manipulation of the composition of Ni-rich layered cathode for the design of cathodes with high energy density and safety.

all-solid-state batteries adjusting to the requirements for both high safety and energy density,^[2] the material design of other thermally stable battery components besides the electrolyte should also be considered. Increasing the energy density of electrode materials generally necessitates high-voltage operation^[3] or the use of Ni-rich Ni–Co–Mn-based oxide (NCM) cathodes for more accessible lithium within the charging cut-off voltage.^[1b,4] However, removing more lithium from the cathode results in a thermodynamically unstable phase that can be easily decomposed and undergo a phase transition during O_2 evolution,^[5] thereby increasing the risk of thermal explosion.^[5a,6] Thus, high thermal structural stability of the cathode materials is needed to ensure the safety of lithium rechargeable batteries.^[5b,6a,7]

1. Introduction

Rechargeable batteries with high safety have attracted tremendous attention in the effort to address ever-increasing energy demands, as they can serve as a power source for electric vehicles and as an energy buffer between sustainable yet intermittent energy resources (i.e., solar and wind energies) and the load.^[1] Given the general trend in the development of

The thermal stability and structural evolution of commercially available NCM cathode materials has been widely investigated.^[5a,6–8] Combined analysis using in situ X-ray diffraction (XRD) or absorption spectroscopy (XAS) and transmission electron microscopy (TEM) has revealed that the vulnerable phase stability of a charged cathode induces gradual structural evolution at high temperature. As the temperature increases from 25 to 600 °C, a rhombohedral ($R\bar{3}m$) to spinel ($Fd\bar{3}m$) to rock-salt phase ($Fm\bar{3}m$) transition was observed accompanied by

S.-K. Jung, K. Kang
Department of Materials Science and Engineering
Research Institute of Advanced Materials (RIAM)
Seoul National University
Seoul 08826, Republic of Korea
E-mail: skjung@unist.ac.kr; matlgen1@snu.ac.kr

S.-K. Jung, K. Kang
Center for Nanoparticle Research
Institute for Basic Science (IBS)
Seoul 08826, Republic of Korea

S.-K. Jung
Department of Energy Engineering
School of Energy and Chemical Engineering
Ulsan National Institute of Science and Technology (UNIST)
Ulsan 44919, Republic of Korea

H. Kim, S. H. Song, S. Lee
Korea Atomic Energy Research Institute (KAERI)
111 Daedeok-daero 989 Beon-Gil, Yuseong-gu, Daejeon 34057,
Republic of Korea

S. H. Song
Department of Chemical and Biological Engineering
Korea University
145 Anam-Ro, Seongbuk-Gu, Seoul 02841, Republic of Korea

J. Kim
Department of Energy Science
Sungkyunkwan University
Suwon 16419, Republic of Korea

 The ORCID identification number(s) for the author(s) of this article can be found under <https://doi.org/10.1002/adfm.202108790>.

DOI: 10.1002/adfm.202108790

transition-metal migration and O₂ evolution.^[6] Most NCM cathodes follow the layered-to-spinel-to-rock-salt phase-transition route regardless of the composition; however, the onset temperature of the phase transition and O₂ emission gradually decrease upon increasing the Ni content from 40 at% (NCM433) to 80 at% (NCM811).^[6b] In addition, the phase transition of Li_{0.33}Ni_{1/3}Co_{1/3}Mn_{1/3}O₂ (NCM111) was shown to be relatively delayed compared with that of Li_{0.33}Ni_{0.8}Co_{0.15}Al_{0.05}O₂ (NCA) ($\approx 340^\circ\text{C}$ vs $\approx 250^\circ\text{C}$).^[6a] These results imply the veiled role of the transition-metal ion in the structural evolution and decomposition reaction upon O₂ emission at high temperature in NCM materials.

The element-dependent transition-metal migration during the phase transition has been indirectly investigated through combined XAS and extended X-ray absorption fine structure (EXAFS) analysis.^[8d,9] It has been suggested that both Ni and Mn are preferentially located in octahedral sites of the rock-salt or layered structure and that Co mainly occupies the tetrahedral site of the spinel phase during the phase transition. The reduction of Ni⁴⁺ to Ni²⁺ due to the oxygen emission implies that Ni can easily migrate to the Li layer to form the rock-salt phase owing to the similar ionic radii of Ni²⁺ (69 pm) and Li⁺ (76 pm). In addition, the oxidation state of Mn is maintained as Mn⁴⁺ upon heating, which implies that Mn is a structural stabilizer that can enhance the thermal stability. The Co ion has also been regarded as a structure stabilizer that delays the rock-salt phase transition via the formation of a spinel phase of similar local environment to the M₃O₄-type spinel.^[5b,6b,9c] The role of each transition-metal ion in the thermal stability is thus far understood mainly in terms of structural evolution.

The role of the transition-metal ion in the thermal stability has recently been studied in terms of oxygen emission.^[10] Liu et al. compared the role of Co and Mn in the thermal stability by varying the composition in high-Ni cathode materials with fixed composition of Ni to decouple the Ni effect on the thermal stability. They resolved that Co exhibits a more positive effect on safety than Mn with evidence of a smaller amount of oxygen emission at $\approx 250^\circ\text{C}$ for the Co-rich phase compared with the Mn-rich phase. As a next step, the role of each transition-metal ion in the correlation between the formation of the evolved phase and O₂ emission requires in-depth understanding to provide clear guidance for the design of cathode materials with both high energy density and safety. However, the conventional structural analysis using XRD applied thus far for studying the thermal decomposition behavior has the limitation that the effects of Ni, Co, and Mn cannot be distinguished because of their similar electron densities and atomic scattering factors; likewise, TEM analysis can only provide local information at the particle surfaces.

In the current work, we investigated the thermal migration of Ni, Co, and Mn ions in Li_xNi_{0.5}Co_{0.2}Mn_{0.3}O₂ ($x = 0.5, 0.33$) (NCM523) and the effect of their migration on the structural transition and O₂ evolution using combined in situ neutron diffraction (ND) and gas analyses. Neutron diffraction is powerful structural analysis tool that complements XRD by enabling to observe the lithium and distinguish neighboring atoms in periodic table due to different nuclear scattering length of neutrons.^[11] We selected NCM523 as a representative Ni-rich cathode containing sufficient amounts of Co and Mn for

reliable analysis. The thermal migration of Ni, Co, and Mn ions upon phase transition, including the correlation between the thermal migration and phase transition with the O₂ evolution as a function of Li content, were quantitatively analyzed. We observed that the migration of Co ions, which depends on the Li content in Li_xNi_{0.5}Co_{0.2}Mn_{0.3}O₂ ($x = 0.5, 0.33$), is related to the O₂ evolution during the formation of the spinel phase. We identified the role of Co ions in both the phase transition and the evolution of oxygen gas in NCM materials, and our findings fill the gap of understanding of the role of Co in the correlation between phase transition and oxygen emission. The results of this study improve our understanding of the roles of Ni, Co, and Mn in NCM materials in delivering thermal stability and provide intuition for the design of cathodes with high safety.

2. Results and Discussion

2.1. Synthesis and Characterization

of Li_xNi_{0.5}Co_{0.2}Mn_{0.3}O₂ ($x = 1.0, 0.8, 0.6, 0.5, 0.33$)

We synthesized Li_xNi_{0.5}Co_{0.2}Mn_{0.3}O₂ (NCM523) using a chemical delithiation method with NO₂BF₄ as a strong oxidizing agent to investigate the thermal atomic migration in charged NCM523 materials. **Figure 1a,b** presents the synchrotron XRD and ND patterns of Li_xNi_{0.5}Co_{0.2}Mn_{0.3}O₂ ($x = 1.0, 0.8, 0.6, 0.5, 0.33$), which do not show any trace of impurities. The state of charge (SOC) of each sample was confirmed by Rietveld refinement of the XRD, ND, and inductively coupled plasma atomic emission spectroscopy (ICP-AES) results, as shown in Figures S1–S2 and Table S1 (Supporting Information). The equivalent voltage for chemically delithiated samples is presented in Figure S3 (Supporting Information). **Figure 1c,d** shows the lattice parameter changes upon delithiation, which indicate that the *a* lattice parameter and lattice volume decrease upon Li extraction while the *c* lattice parameter increases. This result is consistent with previous findings.^[12] The decrease of the *a* lattice parameter is due to the contraction of the TM–O bond (TM = Ni, Co, or Mn) in the octahedra caused by oxidation as the lithium content decreases in NCM523, as illustrated in **Figure 1e**. For the *c* lattice parameter, the Li-deficient state induced stronger electrostatic repulsion between the two opposing oxygen layers across the van der Waals gap, resulting in increases of the Li–O bond length and *c* lattice parameter. The TM and Li slab spaces as a function of Li content in Li_xNi_{0.5}Co_{0.2}Mn_{0.3}O₂ are presented in **Figure S4** (Supporting Information). Ni migration from the octahedral site in the TM (TM_{oct}) layer to the octahedral site in the Li layer (Li_{oct}) and the subsequent spinel-phase formation were confirmed in a highly charged state of Li_xNi_{0.5}Co_{0.2}Mn_{0.3}O₂ ($x = 0.5, 0.33$) by ND analyses. Note that ND analysis enables us to investigate the Li site and occupancy in the lattice and to distinguish neighboring transition metals such as Ni, Co, and Mn because of the different coherent nuclear scattering lengths of the neutrons (Li = -1.9 fm, Ni = 10.3 fm, Co = 2.49 fm, Mn = -3.73 fm).^[13] The Ni occupancy in Li_{oct} sites remained below 3.0% until 0.4 Li extraction and then increased to 4.4% in the charged state of Li_{0.33}Ni_{0.5}Co_{0.2}Mn_{0.3}O₂, as observed in **Figure 1f**. The presence of ≈ 1.7 and 3.2 wt% of the crystalline *Fd3m* spinel phase was

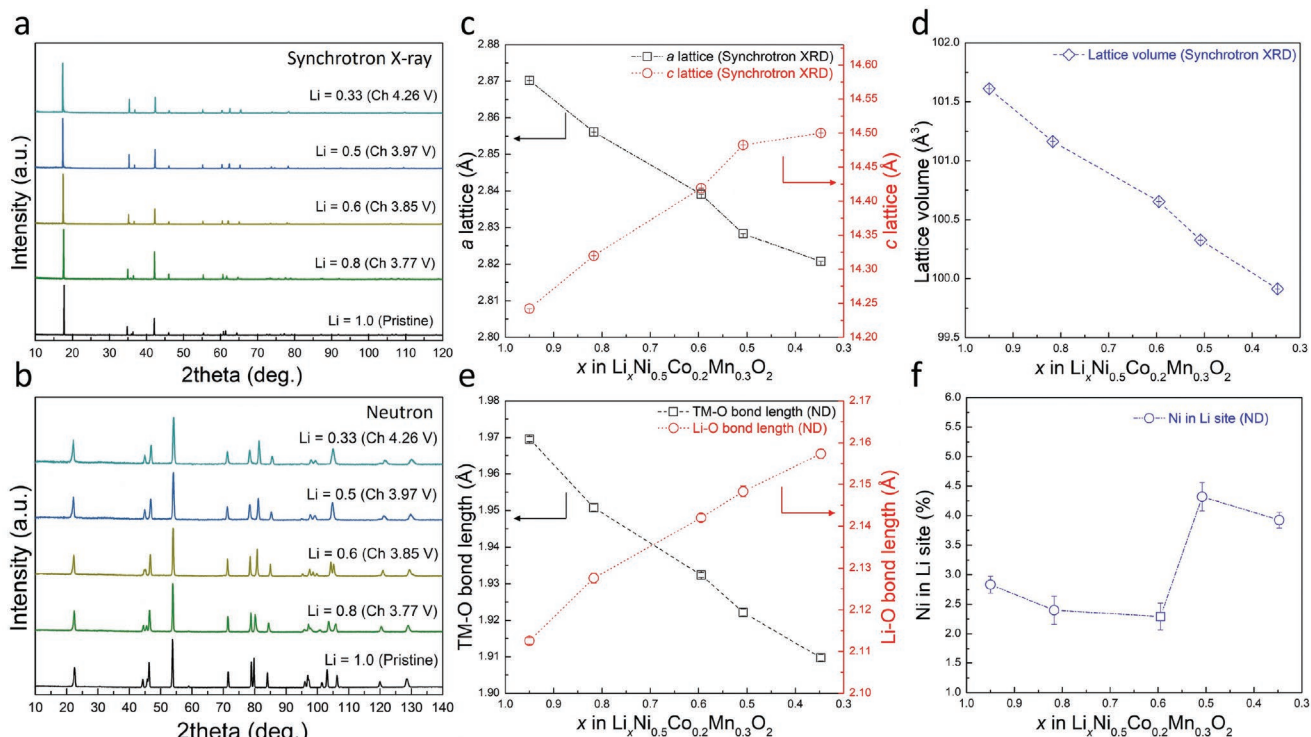


Figure 1. a) Synchrotron X-ray and b) neutron powder diffraction patterns of $\text{Li}_x\text{Ni}_{0.5}\text{Co}_{0.2}\text{Mn}_{0.3}\text{O}_2$ ($x = 1.0, 0.8, 0.6, 0.5, 0.33$). c) Lattice parameters and d) cell volume changes in $\text{Li}_x\text{Ni}_{0.5}\text{Co}_{0.2}\text{Mn}_{0.3}\text{O}_2$ analyzed by Rietveld refinement of synchrotron X-ray diffraction data. e) TM–O and Li–O bond lengths (TM, where TM = Ni, Co, or Mn) as a function of Li content from neutron diffraction analysis. f) Ni occupancy in Li octahedral sites upon Li extraction from neutron diffraction analysis.

confirmed for $\text{Li}_x\text{Ni}_{0.5}\text{Co}_{0.2}\text{Mn}_{0.3}\text{O}_2$ ($x = 0.5, 0.33$), respectively, by Rietveld refinement, and a trace of the spinel phase was also detected in the TEM selected area electron diffraction pattern, as shown in Figure S5 (Supporting Information).

2.2. Structural Change and Gas Evolution in $\text{Li}_x\text{Ni}_{0.5}\text{Co}_{0.2}\text{Mn}_{0.3}\text{O}_2$ ($x = 0.5, 0.33$) at High Temperature

We first studied the global structural evolution using in situ high-temperature ND analysis coupled with gas mass spectroscopy to investigate the atomic thermal migration and oxygen stability of the charged electrodes of $\text{Li}_x\text{Ni}_{0.5}\text{Co}_{0.2}\text{Mn}_{0.3}\text{O}_2$ ($x = 0.5, 0.33$) at high temperatures. The temperature was increased from RT to 600 °C in intervals of 40 °C or 50 °C at a heating rate of 10 °C min^{-1} , and the temperature was maintained for 10 min at each step before the ND measurement. As observed in Figure 2a,b, the phase transition from the layered ($R\bar{3}m$) to spinel ($Fd\bar{3}m$) to rock-salt ($Fm\bar{3}m$) structure upon increasing the temperature is apparent in the contour plots of the ND patterns of $\text{Li}_x\text{Ni}_{0.5}\text{Co}_{0.2}\text{Mn}_{0.3}\text{O}_2$ ($x = 0.5, 0.33$). The first phase transition from the layered to spinel phase in $\text{Li}_{0.5}\text{Ni}_{0.5}\text{Co}_{0.2}\text{Mn}_{0.3}\text{O}_2$ was clearly detected at 350 °C, with the $(018)_L$ and $(110)_L$ diffraction peaks shifting toward each other and merging into the $(440)_S$ peak. In addition, gradual formation of the rock-salt phase was observed after 470 °C. These structural changes were easily confirmed by other diffraction peaks in various 2θ ranges, as shown in Figure S6a,b

(Supporting Information). The phase-transition temperatures from the layered to spinel and spinel to rock-salt phases for $x = 0.33$ were 40–50 °C lower than those for $x = 0.5$ because of the low stability of overcharged NCM materials, as shown in Figure 2b and Figure S6c,d (Supporting Information).^[5] The earlier phase transition from layered to spinel phase in $x = 0.33$ sample and sudden drastic peak evolution from $(110)_L$ to $(440)_S$ compared to $x = 0.5$ sample is attributed to the low thermal structural stability involving severe O_2 gas evolution as well as Ni and Co migration, which will be discussed later section. Structural evolution upon subsequent cooling was further investigated using in situ high temperature XRD, which indicates that no phase evolution occurred upon subsequent cooling process (see Figure S7: Supporting Information).

The phase fractions of the charged NCM materials ($x = 0.5, 0.33$) were quantitatively determined using Rietveld refinement of the ND patterns to understand the phase transitions at high temperature and their relation to the thermal stability. Figure 2c,d shows the phase fraction of the layered ($R\bar{3}m$), spinel ($Fd\bar{3}m$), and rock-salt ($Fm\bar{3}m$) phases as a function of temperature from 25 °C to 600 °C. The structure of $\text{Li}_{0.5}\text{Ni}_{0.5}\text{Co}_{0.2}\text{Mn}_{0.3}\text{O}_2$ consisting of ≈ 96 wt% of the layered ($R\bar{3}m$) phase of $\text{Li}_{0.5}\text{Ni}_{0.5}\text{Co}_{0.2}\text{Mn}_{0.3}\text{O}_2$ and 4 wt% of the spinel ($Fd\bar{3}m$) phase was maintained up to 230 °C; the fraction of the spinel structure linearly increased from 230 to 470 °C, with the opposite trend observed for the layered $R\bar{3}m$ structure. At 470 °C, the layered ($R\bar{3}m$) phase disappeared, and the rock-salt ($Fm\bar{3}m$) phase started to evolve at 510 °C. The final phase

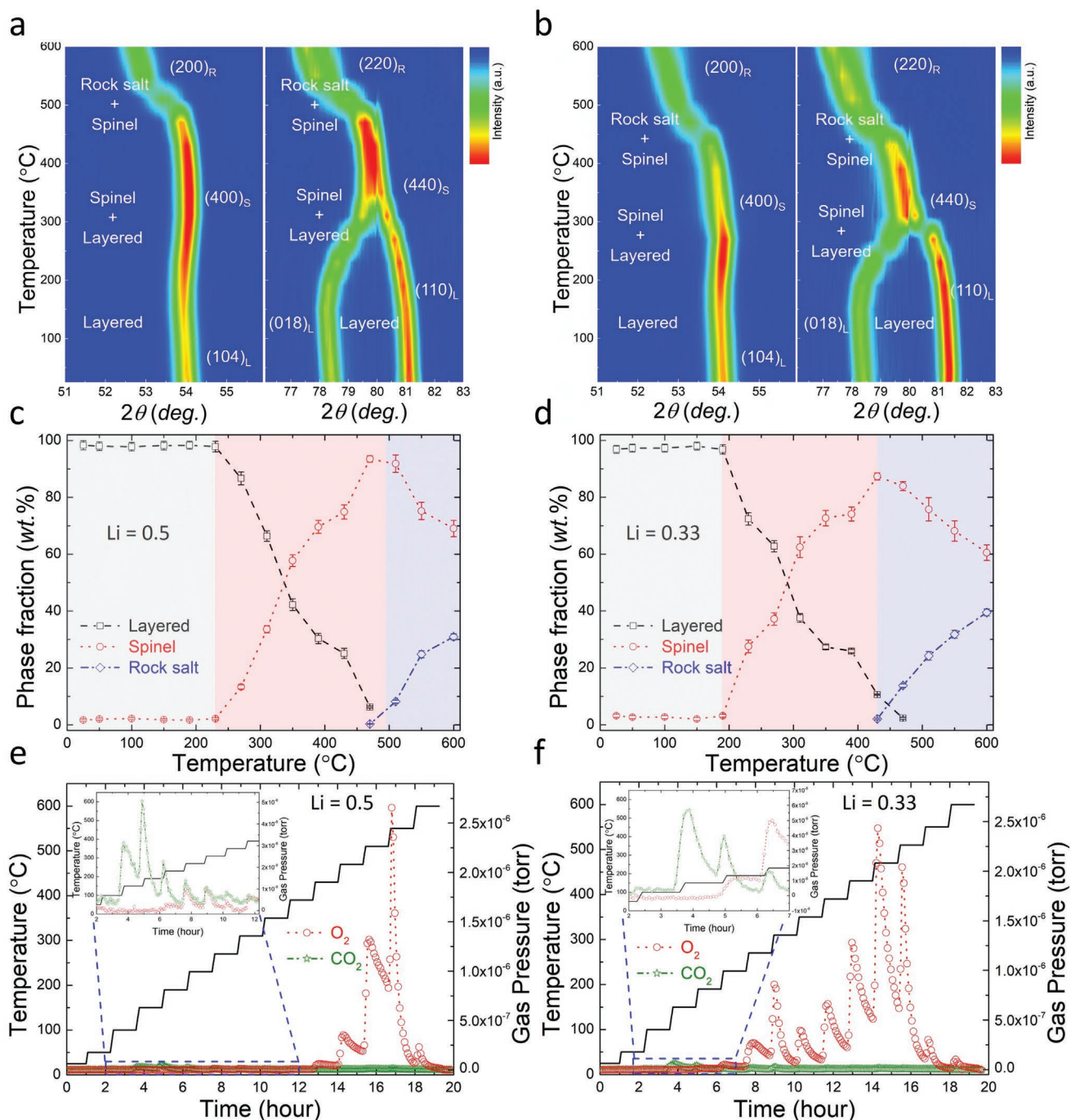


Figure 2. Contour plots of in situ high-temperature neutron diffraction patterns of $\text{Li}_x\text{Ni}_{0.5}\text{Co}_{0.2}\text{Mn}_{0.3}\text{O}_2$ (a) $x = 0.5$, b) $x = 0.33$). Each phase evolved during heating was described as a single-letter abbreviation with its index: layered NCM523 (L), spinel (S), rock-salt (R). Phase fraction of $\text{Li}_x\text{Ni}_{0.5}\text{Co}_{0.2}\text{Mn}_{0.3}\text{O}_2$ (c) $x = 0.5$, d) $x = 0.33$) in the temperature range of 25–600 $^{\circ}\text{C}$. O_2 and CO_2 gases released from $\text{Li}_x\text{Ni}_{0.5}\text{Co}_{0.2}\text{Mn}_{0.3}\text{O}_2$ ((e) $x = 0.5$, f) $x = 0.33$) upon heating to 600 $^{\circ}\text{C}$. The black line represents the temperature as a function of time. The inset figures are magnified images of the low-temperature ranges at which CO_2 evolution occurs.

fraction ratio between the spinel and rock-salt phases at 600 $^{\circ}\text{C}$ was 70:30 (wt%). Similar phase transitions were confirmed for $\text{Li}_{0.33}\text{Ni}_{0.5}\text{Co}_{0.2}\text{Mn}_{0.3}\text{O}_2$ at slightly lower temperatures, as observed in Figure 2d. The spinel phase started to appear at 190 $^{\circ}\text{C}$, and the layered phase completely disappeared at 470 $^{\circ}\text{C}$. The rock-salt phase evolution occurred at 430 $^{\circ}\text{C}$, and

the phase-fraction ratio between the spinel and rock-salt phases at 600 $^{\circ}\text{C}$ was 60:40 (wt%).

To attain a deeper understanding of the atomic-scale structural evolution of $\text{Li}_x\text{Ni}_{0.5}\text{Co}_{0.2}\text{Mn}_{0.3}\text{O}_2$ ($x = 0.5, 0.33$) and its relation to the gas evolution, O_2 and CO_2 gases were captured by a gas analyzer upon heating. Figure 2e,f shows the O_2 and

CO₂ gas evolution from Li_xNi_{0.5}Co_{0.2}Mn_{0.3}O₂ ($x = 0.5, 0.33$) samples as a function of temperature from RT to 600 °C. No significant CO₂ gas emission was detected in the phase-transition temperature range in NCM materials,^[6c] and only small amounts of CO₂ were detected in the low-temperature range of 150 to 230 °C from both Li_xNi_{0.5}Co_{0.2}Mn_{0.3}O₂ ($x = 0.5, 0.33$) electrodes (Figure S8, Supporting Information), which was suspected to originate from the LiOH, Li₂CO₃, and carbon containing impurities that can be formed by the chemical reaction of charged cathode against to air or CO₂ exposure during the sample preparation process.^[14] Notably, the onset temperature of the oxygen-gas evolution strongly depended on the Li content in Li_xNi_{0.5}Co_{0.2}Mn_{0.3}O₂ ($x = 0.5, 0.33$); however, the materials exhibited similar phase-fraction changes with increasing temperature. The release of O₂ started at ≈400 °C in the Li_{0.5}Ni_{0.5}Co_{0.2}Mn_{0.3}O₂ electrode, and a significant amount of O₂ gas was detected from Li_{0.5}Ni_{0.5}Co_{0.2}Mn_{0.3}O₂ in the temperature range of 470–550 °C, which corresponds to the temperature range of the spinel-to-rock-salt phase transition. The onset temperature of O₂ evolution in the Li_{0.5}Ni_{0.5}Co_{0.2}Mn_{0.3}O₂ electrode was relatively higher than that in Li_xNi_{0.8}Co_{0.15}Al_{0.05}O₂ ($0 < x < 1$) (NCA) electrodes, which generate oxygen at ≈200 °C regardless of the Li content; this finding indicates that Mn and Co act as structural stabilizers in the charged state and at high temperature in layered electrode materials.^[5b,6a,c,9c] For the highly charged sample of Li_{0.33}Ni_{0.5}Co_{0.2}Mn_{0.3}O₂, O₂ emission began at a low temperature of 230 °C, and the amount of O₂ evolution continuously increased up to 470 °C. Note that the temperature range of O₂ evolution was consistent with that of the layered-to-spinel and spinel-to-rock-salt transitions. This result was attributed to the different thermal atomic migration behavior in the Li_xNi_{0.5}Co_{0.2}Mn_{0.3}O₂ ($x = 0.5, 0.33$) electrodes, the details of which will be discussed later.

2.3. Atomic Migration and Phase Transition in Li_xNi_{0.5}Co_{0.2}Mn_{0.3}O₂ ($x = 0.5, 0.33$) at High Temperature

To understand the atomic-migration behavior at high temperature and its relation to the phase transition in charged NCM materials, we analyzed in situ high-temperature ND patterns of Li_xNi_{0.5}Co_{0.2}Mn_{0.3}O₂ ($x = 0.5, 0.33$) using Rietveld refinement. We first simulated the ND patterns of Li_{0.5}Ni_{0.5}Co_{0.2}Mn_{0.3}O₂ containing different amounts of Ni, Co, and Mn in the Li_{oct} site (see Figure S9, Supporting Information) to investigate the effect of atomic migration on ND patterns in the layered structure of charged NCM materials. The intensities of the (003) and (006) peaks significantly decreased with increasing Ni or Co content in the Li_{oct} site, with the opposite behavior observed for increasing Mn content. We also considered the oxygen evolution in layered structure by simulating ND patterns of oxygen deficient Li_{0.5}Ni_{0.5}Co_{0.2}Mn_{0.3}O_{2-γ} ($0 < γ < 0.4$). The intensities of (003) and (006) peaks increased as the lattice oxygen gradually decreases to 80% (Figure S9, Supporting Information). A trend of decreasing (003) and (006) peak intensities at high temperature, which is in opposite to the Mn ion migration and oxygen evolution, indicating Ni migration from the TM to Li layer, was observed in the experimental ND patterns of Li_xNi_{0.5}Co_{0.2}Mn_{0.3}O₂ ($x = 0.5, 0.33$), as shown in Figure 3a.

Please note that possibility of Co ion migration from TM layer to Li layer in layered structure is excluded below the phase transition temperature due to the larger octahedral site stabilization energy (OSSE) of low-spin Co³⁺ ion (−21.33 Dq) than that of Ni³⁺ (−12.67 Dq) and Ni²⁺ (−8.44 Dq). The extent of Ni migration from the TM to Li layer was quantified by Rietveld refinement; the Ni occupancies in the Li_{oct} site increased from 4% to 16% for both electrodes upon increasing the temperature to 270 °C, and the Li occupancies in TM_{oct} vanished after 190 °C, as observed in Figure 3b. The peak intensity ratio of the (104) and (003) peaks shown in Figure S10 (Supporting Information) increased with increasing temperature, which is generally regarded as evidence of Ni migration in XRD analysis.^[1h,15] Note that ≈2–3% of Co ion migration was confirmed from Li_{0.33}Ni_{0.5}Co_{0.2}Mn_{0.3}O₂ at temperatures of 230 and 270 °C, while no Co occupancies were found from Li_{0.5}Ni_{0.5}Co_{0.2}Mn_{0.3}O₂. We further analyzed the lattice parameters and cell volume. The *a* and *c* lattice parameters and cell volume increased with increasing temperature up to 150 °C because of the thermal expansion (see Figure S11a,b: Supporting Information). However, sudden decreases in the *c* lattice parameter and cell volume originating from Ni migration from the TM layer to Li layer were observed. Figure S11c (Supporting Information) presents the TM–O bond and Li–O bond length changes during heating up to 270 °C; it is apparent that the TM reduction occurred above 230 °C with an increase of TM–O bond length and decrease of the Li–O bond length. The TM and Li slab spaces showed consistent trends of increasing TM slab space and decreasing Li slab space above 230 °C (see Figure S11d, Supporting Information). Note that significant lattice parameter and Li–O bond length changes during heating up to 270 °C were confirmed from $x = 0.33$ sample, which is attributed to the O₂ gas evolution and metal migration at comparably low temperature. Detailed structural information from Rietveld analysis is presented in Figure S12 and Table S2 (Supporting Information).

The nuclear density maps of Li_xNi_{0.5}Co_{0.2}Mn_{0.3}O₂ ($x = 0.5, 0.33$) obtained using the maximum entropy method (MEM) in Figure 3c and Figure S13 (Supporting Information) further support the Ni migration from TM_{oct} to Li_{oct} and Li migration from Li_{oct} to Li_{tet}. The maps reveal that significant nuclear density from positive neutron scattering, which may originate from Ni or Co, was detected at the Li_{oct} site at 270 °C, whereas no nuclear density from positive neutron scattering in the Li layer was detected at 25 °C (Li = −1.9 fm, Ni = 10.3 fm, Co = 2.49 fm, Mn = −3.73 fm). Additionally, negative neutron scattering signals, which may originate from Li occupancies, were observed for the Li_{tet} sites from both charged NCM materials, Li_xNi_{0.5}Co_{0.2}Mn_{0.3}O₂ ($x = 0.5, 0.33$), at 270 °C. Note that this is the first time that the occupancies of Ni and Li in the octahedral and tetrahedral sites in the Li layer have been directly visualized. Taken together, Ni migration from the TM to Li layer in Li_xNi_{0.5}Co_{0.2}Mn_{0.3}O₂ ($x = 0.5, 0.33$) increases with increasing temperature in the range of RT to 270 °C, and the increase of the Ni concentration in the Li layer causes contraction of the Li slabs and reordering of Ni in the Li layer, resulting in the transition from the layered phase to the LiMn₂O₄-type spinel phase. Detailed information on MEM calculation of Li_xNi_{0.5}Co_{0.2}Mn_{0.3}O₂ ($x = 0.5, 0.33$) were presented in Table S3 (Supporting Information).

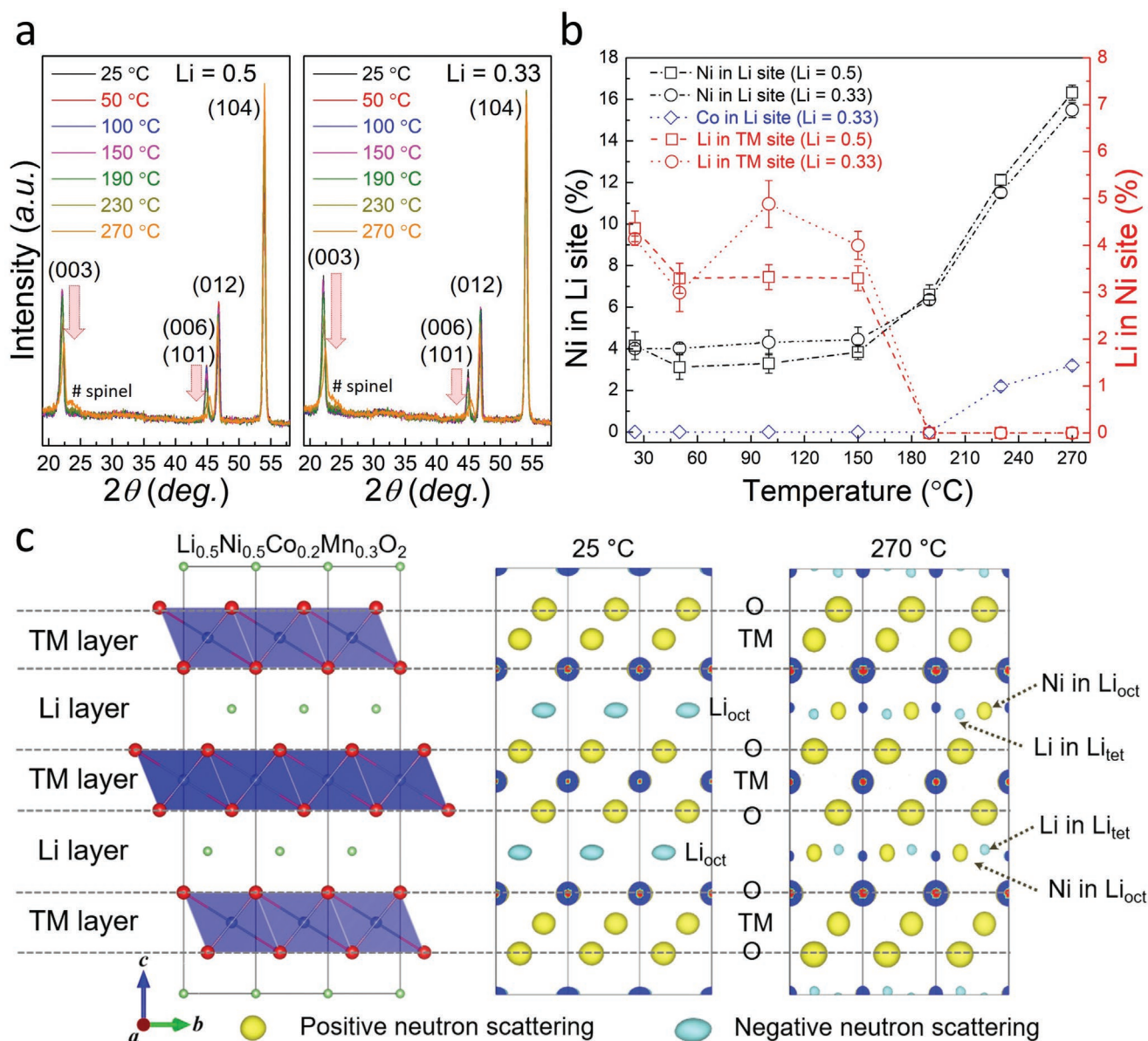


Figure 3. a) Magnified ND patterns of $\text{Li}_x\text{Ni}_{0.5}\text{Co}_{0.2}\text{Mn}_{0.3}\text{O}_2$ ($x = 0.5, 0.33$) in the temperature range of 25–270 °C. b) Ni and Co occupancies in Li_{oct} site and Li occupancies in TM_{oct} sites upon heating from 25 to 270 °C analyzed by Rietveld refinement. c) Nuclear density maps of $\text{Li}_{0.5}\text{Ni}_{0.5}\text{Co}_{0.2}\text{Mn}_{0.3}\text{O}_2$ along [100] projection analyzed using the maximum entropy method. The contours represented by yellow and pale-blue colors indicate the nuclear density from positive and negative neutron scatterings, respectively. (Li = -1.9 fm, Ni = 10.3 fm, Co = 2.49 fm, Mn = -3.73 fm).

The spinel phase, which transformed from the layered structure with the TM migration, has two types of structures depending on the local environment of the TM ion. One structure is the LiM_2O_4 -type spinel with the TM occupying the octahedral site in the Li layer, and the other structure is the M_3O_4 -type spinel with the TM occupying both the octahedral site and adjacent tetrahedral site in the Li layer.^[6b,16] We quantitatively analyzed the formation of the LiM_2O_4 - and M_3O_4 -type spinel structures using Rietveld refinement of ND patterns. First, ND patterns of the $Fd\bar{3}m$ spinel were simulated depending on the Ni, Co, and Mn occupancies in the tetrahedral site in the Li layer, as shown in Figure S14 (Supporting Information). The (111) and (400) peak intensities significantly decreased with

increasing Ni or Co contents in the tetrahedral site in the Li layer. In contrast, these peaks increased with increasing Mn occupancy. With increasing temperature, the (111) and (400) peak intensities in the experimental ND patterns significantly decreased, which may have resulted from migration of Ni or Co from the TM octahedral site to the Li tetrahedral site, as observed in Figure 4a,b (Supporting Information). Notably, a clear difference was observed between the two phases of $\text{Li}_x\text{Ni}_{0.5}\text{Co}_{0.2}\text{Mn}_{0.3}\text{O}_2$ ($x = 0.5, 0.33$). The intensity of the (400) diffraction peak gradually decreased from 270 °C to 470 °C for the $x = 0.33$ sample, whereas a sudden decrease of the (400) peak intensity was detected at 470 °C for the $x = 0.5$ sample. A similar trend was observed for the O_2 evolution behavior in

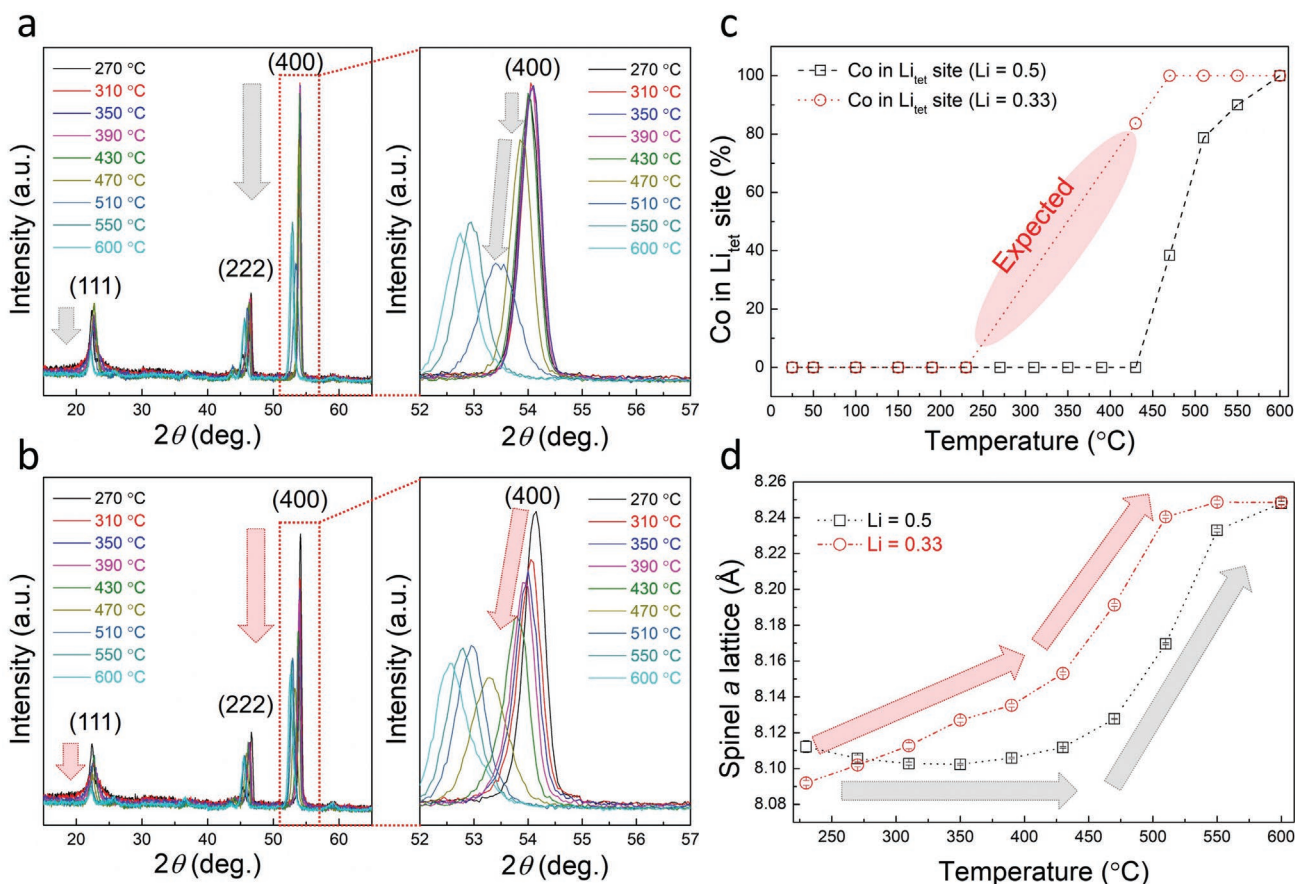
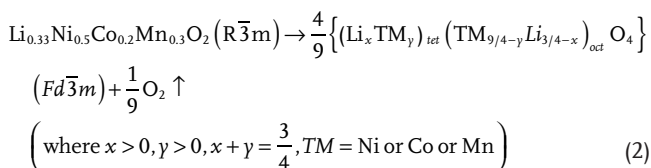
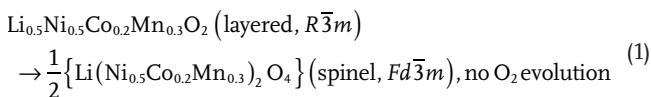


Figure 4. Magnified ND patterns of $\text{Li}_x\text{Ni}_{0.5}\text{Co}_{0.2}\text{Mn}_{0.3}\text{O}_2$ (a) $x = 0.5$, b) $x = 0.33$) in the temperature range of 270–600 °C. c) Co occupancies in Li_{tet} site and d) lattice parameters of $Fd\bar{3}m$ spinel upon heating from 270 to 600 °C analyzed by Rietveld refinement.

$\text{Li}_x\text{Ni}_{0.5}\text{Co}_{0.2}\text{Mn}_{0.3}\text{O}_2$ ($x = 0.5, 0.33$) at high temperature, with little difference in the phase fraction from the layered to spinel structure (see Figure 2). For $x = 0.33$, the layered-to-spinel transition was accompanied by O_2 evolution; however, no oxygen-gas emission was detected for the $x = 0.5$ sample. This finding indicates different phase evolution routes, including the migration of the transition metals, for the $x = 0.5$ and 0.33 samples:



Given the chemical formulas of the phase transitions of $\text{Li}_x\text{Ni}_{0.5}\text{Co}_{0.2}\text{Mn}_{0.3}\text{O}_2$ ($x = 0.5, 0.33$), the $x = 0.5$ sample was expected to transform into a LiM_2O_4 -type spinel without O_2 evolution, whereas the $x = 0.33$ sample was expected to transform into a M_3O_4 -type spinel with O_2 evolution. Note that a significant amount of Co migration ($\approx 84\%$) was observed at a comparably

low temperature of 430 °C for the $x = 0.33$ sample, whereas that in the $x = 0.5$ sample at 510 °C was $\approx 79\%$, as shown in Figure 4c. The expected line of Co migration between 230 and 430 °C is indicated. We attempted to quantify the TM migration to Li_{tet} in the $Fd\bar{3}m$ spinel structure using Rietveld refinement; however, it was difficult to distinguish the TM migration into Li_{tet} in the $x = 0.33$ sample in the temperature range of 270–390 °C because of the low phase fraction of spinel phases in the mixed phases of $R\bar{3}m$ and $Fd\bar{3}m$ and thermal atomic disorder, including Li–TM mixing and oxygen deficiency. Nevertheless, we examined the Co migration and subsequent phase transition to the M_3O_4 -type spinel phase by analyzing the lattice parameter of the spinel phase upon heating, as shown in Figure 4d. The a lattice parameter of the $x = 0.5$ sample did not change until 430 °C, whereas it continued increasing with increasing temperature for the $x = 0.33$ sample. We believe that the continuous Co migration from the $x = 0.33$ sample induces the phase transition from the layered to M_3O_4 -type spinel phase, resulting in the continuous lattice parameter change of the spinel phase. Detailed structural information from Rietveld analysis in the temperature range of 270–600 °C is presented in Figure S15 and Table S2 (Supporting Information). The X-ray absorption near edge spectra (XANES) and EXAFS analyses in Figure S16a–c (Supporting Information) further support the formation of the Co_3O_4 -type spinel at high temperature. The

Co K-edge XANES spectra shifted to the low-energy region after being aged at 600 °C, indicating the reduction of Co. The Co EXAFS spectrum showed characteristic peak evolution over 3 Å after aging. The EXAFS signal in the 4–6 Å range is affected by multiple scattering, thus quantitative analysis with EXAFS fitting is needed to describe local structure. However, it is hard to get reliable fitting results, especially for long range ordering (4–6 Å) by considering the both multiple scattering factor and phase fraction of rock salt and spinel phase together. Instead of quantitative analysis, we compared the EXAFS spectra of aged samples with reference EXAFS spectra of spinel and rock salt phase (Co_3O_4 , LiMn_2O_4 , and NiO). As a result, the local environment of Co from the EXAFS spectrum of the aged sample was similar to that of the Co_3O_4 -type spinel. These results are consistent with those of previous in situ XAS studies on charged NCM materials.^[6a,c]

The spinel-to-rock-salt phase transition started to occur at 470 °C and 430 °C for the $\text{Li}_x\text{Ni}_{0.5}\text{Co}_{0.2}\text{Mn}_{0.3}\text{O}_2$ ($x = 0.5, 0.33$) electrodes, respectively. New ND peaks corresponding to the $Fm\bar{3}m$ rock-salt structure (i.e., $(200)_R$, $(220)_R$, $(111)_R$, $(311)_R$, $(222)_R$, and $(400)_R$) evolved at high temperature, as observed in Figure 2 and Figure S6 (Supporting Information); in addition, significant O_2 evolution was detected during the phase transition in both cases, as observed in Figure 2. The oxidation state of each transition metal was investigated using XANES analysis, as shown in Figures S16–S18 (Supporting Information).

The findings indicate that the oxidation state of Ni was reduced after aging the sample at 600 °C because of the formation of the rock-salt phase of NiO, whereas negligible change was observed for Mn. We investigated the local environment of the transition-metal ion using EXAFS analysis. Regardless of the lithium content, both the $x = 0.5$ and 0.33 samples exhibited similar local structures of the Ni, Co, and Mn transition-metal ions. After aging at 600 °C, the local environment of Ni was confirmed to be similar to that of the rock-salt phase of NiO; however, the M_3O_4^- and LiM_2O_4 -type spinel local structures were observed for Co and Mn, respectively. These results are consistent with those of previous in situ XAS studies on charged NCM materials.^[6a,8d,9c]

2.4. Discussion

The major difference in the thermal phase stabilities of the $x = 0.5$ and 0.33 samples of $\text{Li}_x\text{Ni}_{0.5}\text{Co}_{0.2}\text{Mn}_{0.3}\text{O}_2$ was mainly related to whether the phase transition from the layered-to-spinel phase in the range of 270–470 °C involved Co migration and subsequent O_2 evolution, as shown in Figure 5. Whereas Co migration and O_2 evolution were barely detected in the $x = 0.5$ sample in this temperature range, a significant amount of O_2 was evolved with Co migration in the $x = 0.33$ sample, indicating that the oxygen-deficient M_3O_4 -type spinel phase was

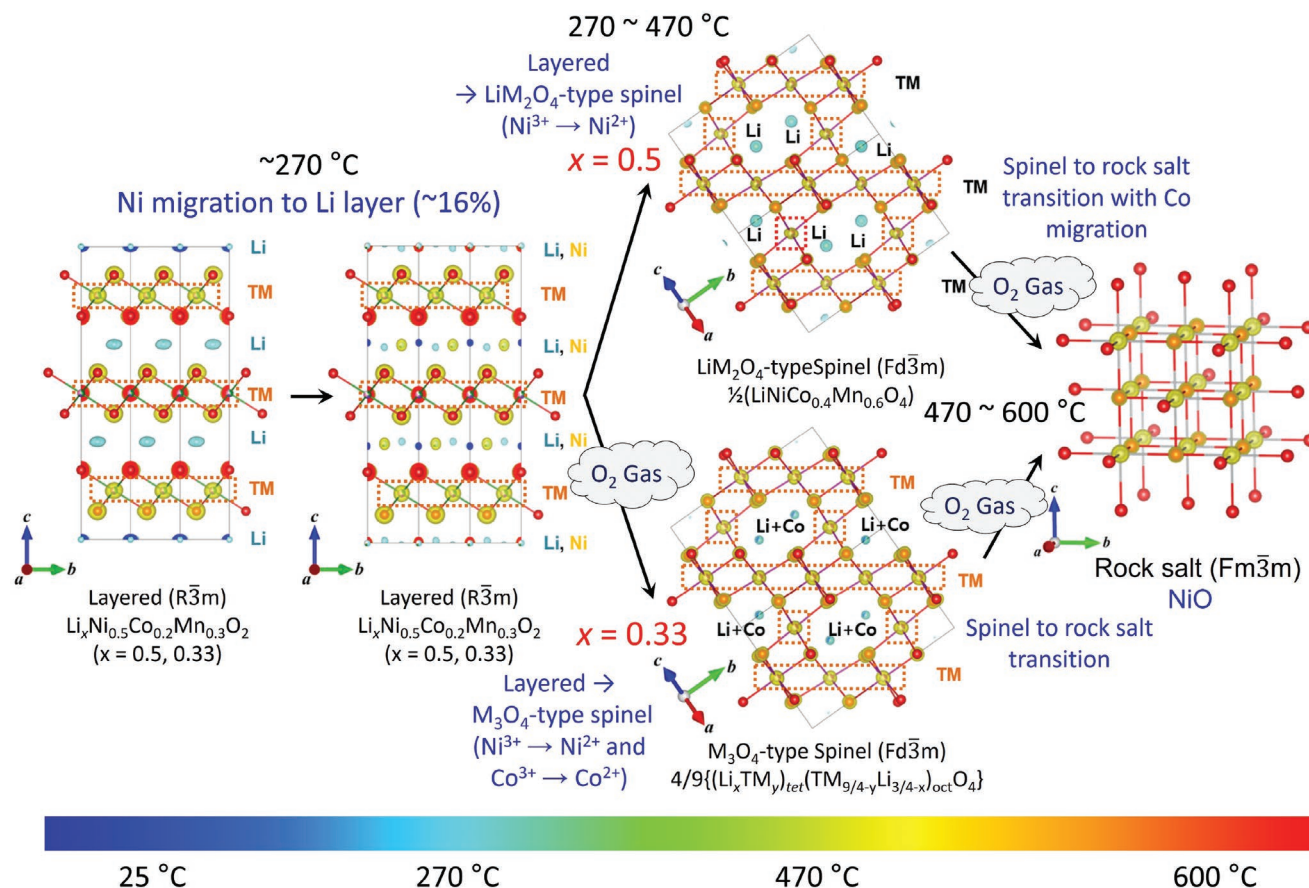


Figure 5. Schematic representation of phase transition from layered to spinel to rock-salt structure in $\text{Li}_x\text{Ni}_{0.5}\text{Co}_{0.2}\text{Mn}_{0.3}\text{O}_2$ ($x = 0.5, x = 0.33$).

formed. This phase evolution cannot be fully understood by the generally accepted claim that an increase of $\text{Ni}^{4+}\text{-O}^{2-}$ bonding with covalent character makes oxygen release more feasible in a highly charged state in NCM materials.^[17] Because this explanation implies an energetically preferred Ni^{4+} to Ni^{2+} reduction, it cannot explain the Co migration to the tetrahedral site of Li, which must be accompanied by $\text{Co}^{3+}/\text{Co}^{2+}$ reduction. Therefore, oxygen evolution accompanying spinel-phase formation in the range of 270–470 °C indicates that not only the effect of Ni^{4+} to Ni^{3+} or Ni^{2+} reduction but also that of Co^{3+} to Co^{2+} reduction should be considered.

The formation of M_3O_4 -type spinel is induced by the preferential occupation of the Co^{2+} ion in the tetrahedral site of Li, which corroborates the reduction of Co. During the initial oxygen evolution at low temperature (270–400 °C), the reduction of Ni^{4+} to Ni^{3+} or Ni^{2+} and Co^{3+} to Co^{2+} is expected, as observed in the in situ XAS analysis of charged high-Ni NCM cathodes.^[10] We considered the contribution of Ni^{3+} , Ni^{2+} , and Co^{2+} to the formation of M_3O_4 -type spinel, especially tetrahedral site occupation. Given the change in the ND peak intensity in contrast to the simulated pattern with tetrahedral site occupation of Mn (Figure 4 and Figure S14: Supporting Information), the contribution of Mn in M_3O_4 -type spinel is considered to be minor. Among the ions, Ni^{2+} is well known to preferentially occupy the octahedral site of the Li layer, as confirmed in Figure 3b, indicating that tetrahedral-site occupation of Ni^{2+} is insignificant. In terms of the octahedral-site stabilization energy (OSSE), both Ni^{3+} and Co^{2+} have the same OSSE of -12.67 Dq by assuming the low-spin state, as they have the same electron configuration corresponding to $[\text{Ar}]3d^7$. However, tetrahedral coordination of Ni^{3+} appears to be unfavorable given the absence of reports; therefore, occupation of the tetrahedral site by Co^{2+} is more favorable. By comparing the occupancy of Co ions in the spinel phase near the temperature at which the spinel phase transforms into the rock-salt structure, it was experimentally confirmed that the spinel formation accompanying the oxygen evolution is mainly contributed by the Co ion migration (84%, 430 °C from $x = 0.33$) compared with the case without oxygen release (79%, 510 °C from $x = 0.5$).

These results suggest that Co plays a critical role in determining the thermal decomposition route in the NCM series layered cathode materials and can mitigate oxygen evolution and rock-salt phase transition. This phase-transition behavior from the layered to rock-salt phase via the spinel phase is also similarly observed in Ni–Mn-based layered cathode materials. Co and Mn can be regarded as structural stabilizers of the spinel phase, delaying the phase transition from the spinel to rock-salt phase and oxygen evolution.^[5b,6b,7,9c,18] However, the role of Co and Mn in the spinel-phase formation accompanying oxygen evolution should be understood separately. In Ni–Mn layered cathodes, Mn enables the formation of a spinel phase with similar lattice parameter as the NiMn_2O_4 phase;^[7] however, it must be induced by Ni^{2+} or Mn^{2+} migration to the tetrahedral site of Li given the OSSE of Ni (Ni^{2+} : -8.44 Dq, Ni^{3+} : -12.67 Dq, Ni^{4+} : -21.33 Dq) and Mn (Mn^{2+} : 0 Dq, Mn^{3+} : -4.22 Dq, Mn^{4+} : -8.44 Dq). Considering that the tetrahedral sites in NiMn_2O_4 are mainly occupied in the order of Mn^{2+} (78%), Ni^{2+} (12%), Mn^{3+} (10%),^[19] the Mn stabilizer induces spinel formation by the reduction of Ni^{4+} to Ni^{2+} and Mn^{4+} to Mn^{2+} , indicating that

the extent of oxygen evolution during spinel formation could be larger than that during the reduction from Co^{3+} to Co^{2+} due to the participation of more electrons. Larger amounts of oxygen loss could accelerate the phase transition to the rock-salt phase and decrease the onset temperature. Co-rich high-Ni NCM cathodes have been reported to exhibit less oxygen release, a higher onset temperature of phase transition, and less evolution of Mn^{2+} compared with the Mn-rich phase.^[10] Compared with lithium nickel oxide, which undergoes phase transition from the layered to rock salt phase barely through the spinel phase,^[20] Co and Mn can participate as structural stabilizers by delaying the spinel-to-rock-salt phase transition and oxygen evolution. However, Co more effectively mitigates the oxygen release and rock-salt phase transition by allowing the Co^{2+} reduction and Mn_3O_4 -type spinel phase formation.

Potentially, spin transition of the Co ion at a certain temperature during thermal decomposition could accelerate Co migration. When accompanying the phase transition with oxygen evolution, the lattice parameter of the spinel phase gradually increased for the $x = 0.33$ sample, whereas that for the $x = 0.5$ sample remained nearly constant in the range of 270–470 °C. This result may be due to not only the thermal expansion but also the low-spin to high-spin transition of the Co^{3+} ion in the Co_3O_4 -type spinel. Above 600 K, a second-order low-spin to high-spin transition of the octahedral Co^{3+} ion in Co_3O_4 occurs.^[21] This transition could affect an anomalous increase of the lattice parameter due to the larger ionic radius of the high-spin Co^{3+} ion (0.061 nm) relative to that of the low-spin Co^{3+} ion (0.053 nm). An increase of the lattice parameter was observed in the 330–450 °C range (0.25%), which is slightly larger than the increase due to spin transition (0.1%). In addition, this transition can cause variation of the OSSE of the Co^{3+} ion. For the low-spin state, the OSSE of the Co^{3+} ion is -21.33 Dq; however, this value changes to -1.33 Dq in the high-spin state, which indicates that the high-spin state of the Co^{3+} ion can more easily migrate to another octahedral site (such as the lithium site) than the low-spin Co^{3+} ion. The feasibility Co migration to Li_{oct} site that can be induced by low-spin to high-spin transition of the octahedral Co^{3+} ion in layered structure of $\text{Li}_{0.33}\text{Ni}_{0.5}\text{Co}_{0.2}\text{Mn}_{0.3}\text{O}_2$ may promote the formation of M_3O_4 -type spinel phase.

3. Conclusion

The phase evolution of NCM523 electrodes during thermal decomposition was investigated at the atomic scale using combined in situ ND and gas analyses. Our results indicate that NCM523 followed different phase transition routes from a layered to spinel phase depending on its state of charge. In the highly delithiated state ($\text{Li} = 0.33$), the formation of Co_3O_4 -type spinel accompanied by oxygen evolution was observed mainly due to Co-ion migration from octahedral sites in the transition-metal layer to tetrahedral sites in the Li layers. This finding provides new insight into the role of Co ions in the thermal decomposition of NCM523. In particular, Co_3O_4 -type spinel-phase transition inevitably accompanies $\text{Co}^{3+}/\text{Co}^{2+}$ reduction, which could be more effective in mitigating the oxygen release and delaying the rock-salt phase transition compared with Co-free Ni–Mn or Ni-based layered cathodes. Our study helps

improve our understanding of the role of each transition-metal ion in NCM materials in determining the thermal stability and provides intuition for the design of high-Ni cathode materials with high safety.

4. Experimental Section

Synthesis of $\text{Li}_x\text{Ni}_{0.5}\text{Co}_{0.2}\text{Mn}_{0.3}\text{O}_2$ ($x = 1.0, 0.8, 0.6, 0.5, 0.33$): The $\text{LiNi}_{0.5}\text{Co}_{0.2}\text{Mn}_{0.3}\text{O}_2$ powder sample was supplied by Samsung Fine Chemicals (Daejeon, Republic of Korea). Charged powder samples of $\text{Li}_x\text{Ni}_{0.5}\text{Co}_{0.2}\text{Mn}_{0.3}\text{O}_2$ ($x = 0.8, 0.6, 0.5, 0.33$) were prepared using the chemical delithiation method with the use of NO_2BF_4 (Aldrich, 95%) as a strong oxidant and acetonitrile (Sigma–Aldrich, anhydrous 99.8%) as a solvent.^[22] Stoichiometric amounts of the $\text{LiNi}_{0.5}\text{Co}_{0.2}\text{Mn}_{0.3}\text{O}_2$ and NO_2BF_4 were mixed in acetonitrile, and the mixture was aged at 70 °C for 12 h under magnetic stirring at 300 rpm. The resulting solution was filtered several times using acetone and ethanol and then dried at 110 °C for 3 h.

Structural Characterization of $\text{Li}_x\text{Ni}_{0.5}\text{Co}_{0.2}\text{Mn}_{0.3}\text{O}_2$ ($x = 1.0, 0.8, 0.6, 0.5, 0.33$): The crystal structure of $\text{Li}_x\text{Ni}_{0.5}\text{Co}_{0.2}\text{Mn}_{0.3}\text{O}_2$ ($x = 1.0, 0.8, 0.6, 0.5, 0.33$) was characterized using neutron and synchrotron XRD. The synchrotron XRD data were obtained from beamline 9B at the Pohang Accelerator Laboratory (PAL). The measurements were performed in the 2θ range of 10°–150.5° with a step size of 0.01 and a step time of 7 s using a constant wavelength of 1.4639 Å. The ND data were obtained using a high-resolution powder diffractometer (HRPD) at the HANARO facilities at the Korea Atomic Energy Research Institute (KAERI). The data were collected over the 2θ range of 0°–180° with a step size of 0.05 using a constant wavelength of 1.834333 Å. The atomic ratios of Li, Ni, Co, and Mn were confirmed using ICP-AES (Thermo Jarrel Ash, Polyscan 60E, USA). The crystal structure and particle morphologies were characterized using field-emission transmission electron microscopy (FE-TEM; Techani-F20; FEI, Hillsboro, OR, USA). The valence state and local structure around Ni, Mn, and Co were analyzed using XAS at beamline 8C at PAL. The Ni, Mn, and Co K-edge spectra were collected in transmission mode with an electron energy of 3 GeV and a current of 320 mA. In situ high-temperature ND analyses of $\text{Li}_x\text{Ni}_{0.5}\text{Co}_{0.2}\text{Mn}_{0.3}\text{O}_2$ ($x = 0.5, 0.33$) were conducted using a neutron HRPD equipped with a universal gas analyzer (UGA) (Stanford Research Systems) to detect the amount of O_2 and CO_2 gases evolved from the samples. In situ high temperature XRD analyses of $\text{Li}_x\text{Ni}_{0.5}\text{Co}_{0.2}\text{Mn}_{0.3}\text{O}_2$ ($x = 0.5, 0.33$) were conducted using X-ray diffractometer (Empyrean, Malvern PANalytical) equipped with Cu $K\alpha$ radiation ($\lambda = 1.540598$ Å). The nuclear density distribution of $\text{Li}_x\text{Ni}_{0.5}\text{Co}_{0.2}\text{Mn}_{0.3}\text{O}_2$ ($x = 0.5, 0.33$) was analyzed by MEM using program “Dysnomia”.^[23]

Supporting Information

Supporting Information is available from the Wiley Online Library or from the author.

Acknowledgements

S.-K.J. and H.K. contributed equally to this work. This work was supported by the Center for Nanoparticle Research at Institute for Basic Science (IBS) (IBS-R006-A2) and a National Research Foundation of Korea (NRF) grant funded by the Korea government (MSIT, Ministry of Science and ICT) (No. 2015R1A2A1A10055991) (NRF-2017M2A2A6A05017652). This work was also supported by Samsung Research Funding Center of Samsung Electronics under Project Number SRFC-TA1403-53.

Conflict of Interest

The authors declare no conflict of interest.

Data Availability Statement

The data that supports the findings of this study are available in the supplementary material of this article.

Keywords

in situ analysis, Li-ion batteries, neutron diffraction, oxygen evolution, thermal stability

Received: September 1, 2021

Revised: November 29, 2021

Published online: December 15, 2021

- [1] a) F. Wu, J. Maier, Y. Yu, *Chem. Soc. Rev.* **2020**, *49*, 1569; b) W. Li, E. M. Erickson, A. Manthiram, *Nat. Energy* **2020**, *5*, 26; c) W. Li, B. Song, A. Manthiram, *Chem. Soc. Rev.* **2017**, *46*, 3006; d) A. Konarov, S.-T. Myung, Y.-K. Sun, *ACS Energy Lett.* **2017**, *2*, 703; e) D. Larcher, J. M. Tarascon, *Nat. Chem.* **2015**, *7*, 19; f) J. B. Goodenough, K.-S. Park, *J. Am. Chem. Soc.* **2013**, *135*, 1167; g) J. M. Tarascon, M. Armand, *Nature* **2001**, *414*, 359; h) K. Kang, Y. S. Meng, J. Bréger, C. P. Grey, G. Ceder, *Science* **2006**, *311*, 977; i) B. Dunn, H. Kamath, J.-M. Tarascon, *Science* **2011**, *334*, 928.
- [2] a) J. Janek, W. G. Zeier, *Nat. Energy* **2016**, *1*, 1614; b) K. J. Kim, M. Balaish, M. Wadaguchi, L. Kong, J. L. Rupp, *Adv. Energy Mater.* **2021**, *11*, 2002689.
- [3] J.-N. Zhang, Q. Li, C. Ouyang, X. Yu, M. Ge, X. Huang, E. Hu, C. Ma, S. Li, R. Xiao, *Nat. Energy* **2019**, *4*, 594.
- [4] a) S.-K. Jung, H. Gwon, J. Hong, K.-Y. Park, D.-H. Seo, H. Kim, J. Hyun, W. Yang, K. Kang, *Adv. Energy Mater.* **2014**, *4*, 1300787; b) C. P. Grey, J. M. Tarascon, *Nat. Mater.* **2017**, *16*, 45; c) Y.-K. Sun, S.-T. Myung, B.-C. Park, J. Prakash, I. Belharouak, K. Amine, *Nat. Mater.* **2009**, *8*, 320.
- [5] a) J. Zheng, T. Liu, Z. Hu, Y. Wei, X. Song, Y. Ren, W. Wang, M. Rao, Y. Lin, Z. Chen, J. Lu, C. Wang, K. Amine, F. Pan, *J. Am. Chem. Soc.* **2016**, *138*, 13326; b) Y. Xiqian, H. Enyuan, B. Seongmin, Z. Yongning, Y. Xiao-Qing, *Chin. Phys. B* **2016**, *25*, 018205.
- [6] a) K.-W. Nam, S.-M. Bak, E. Hu, X. Yu, Y. Zhou, X. Wang, L. Wu, Y. Zhu, K.-Y. Chung, X.-Q. Yang, *Adv. Funct. Mater.* **2013**, *23*, 1047; b) S.-M. Bak, E. Hu, Y. Zhou, X. Yu, S. D. Senanayake, S.-J. Cho, K.-B. Kim, K. Y. Chung, X.-Q. Yang, K.-W. Nam, *ACS Appl. Mater. Interfaces* **2014**, *6*, 22594; c) S.-M. Bak, K.-W. Nam, W. Chang, X. Yu, E. Hu, S. Hwang, E. A. Stach, K.-B. Kim, K. Y. Chung, X.-Q. Yang, *Chem. Mater.* **2013**, *25*, 337.
- [7] N. Yabuuchi, Y.-T. Kim, H. H. Li, Y. Shao-Horn, *Chem. Mater.* **2008**, *20*, 4936.
- [8] a) H. Konishi, T. Yuasa, M. Yoshikawa, *J. Power Sources* **2011**, *196*, 6884; b) K.-W. Nam, W.-S. Yoon, X.-Q. Yang, *J. Power Sources* **2009**, *189*, 515; c) Y.-H. Cho, D. Jang, J. Yoon, H. Kim, T. K. Ahn, K.-W. Nam, Y.-E. Sung, W.-S. Kim, Y.-S. Lee, X.-Q. Yang, W.-S. Yoon, *J. Alloys Compd.* **2013**, *562*, 219; d) W.-S. Yoon, O. Haas, S. Muhammad, H. Kim, W. Lee, D. Kim, D. A. Fischer, C. Jaye, X.-Q. Yang, M. Balasubramanian, K.-W. Nam, *Sci. Rep.* **2014**, *4*, 6827; e) F. Lin, I. M. Markus, D. Nordlund, T.-C. Weng, M. D. Asta, H. L. Xin, M. M. Doeff, *Nat. Commun.* **2014**, *5*, 3529; f) P. Yan, J. Zheng, J.-G. Zhang, C. Wang, *Nano Lett.* **2017**, *17*, 3946; g) Z. Chen, Y. Ren, E. Lee, C. Johnson, Y. Qin, K. Amine, *Adv. Energy Mater.* **2013**, *3*, 729; h) L. Wu, K.-W. Nam, X. Wang, Y. Zhou, J.-C. Zheng, X.-Q. Yang, Y. Zhu, *Chem. Mater.* **2011**, *23*, 3953.
- [9] a) S. Hwang, S. M. Kim, S.-M. Bak, B.-W. Cho, K. Y. Chung, J. Y. Lee, W. Chang, E. A. Stach, *ACS Appl. Mater. Interfaces* **2014**, *6*, 15140; b) S. Hwang, S. M. Kim, S.-M. Bak, S. Y. Kim, B.-W. Cho, K. Y. Chung, J. Y. Lee, E. A. Stach, W. Chang, *Chem. Mater.* **2015**, *27*,

- 3927; c) H. Konishi, M. Yoshikawa, T. Hirano, K. Hidaka, *J. Power Sources* **2014**, 254, 338.
- [10] X. Liu, G.-L. Xu, L. Yin, I. Hwang, Y. Li, L. Lu, W. Xu, X. Zhang, Y. Chen, Y. Ren, *J. Am. Chem. Soc.* **2020**, 142, 19745.
- [11] a) G. Liang, C. Didier, Z. Guo, W. K. Pang, V. K. Peterson, *Adv. Mater.* **2020**, 32, 1904528; b) Y. Ren, X. Zuo, *Small Methods* **2018**, 2, 1800064; c) G. Liang, V. K. Peterson, Z. Wu, S. Zhang, J. Hao, C. Z. Lu, C. H. Chuang, J. F. Lee, J. Liu, G. Leniec, *Adv. Mater.* **2021**, 33, 2101413.
- [12] a) S.-T. Myung, F. Maglia, K.-J. Park, C. S. Yoon, P. Lamp, S.-J. Kim, Y.-K. Sun, *ACS Energy Lett.* **2017**, 2, 196; b) C.-H. Shen, Q. Wang, H.-J. Chen, C.-G. Shi, H.-Y. Zhang, L. Huang, J.-T. Li, S.-G. Sun, *ACS Appl. Mater. Interfaces* **2016**, 8, 35323; c) O. Dolotko, A. Senyshyn, M. J. Mühlbauer, K. Nikolowski, H. Ehrenberg, *J. Power Sources* **2014**, 255, 197.
- [13] a) D. Mohanty, A. Huq, E. A. Payzant, A. S. Sefat, J. Li, D. P. Abraham, D. L. Wood, C. Daniel, *Chem. Mater.* **2013**, 25, 4064; b) S. C. Yin, Y. H. Rho, I. Swainson, L. F. Nazar, *Chem. Mater.* **2006**, 18, 1901.
- [14] L. Zou, Y. He, Z. Liu, H. Jia, J. Zhu, J. Zheng, G. Wang, X. Li, J. Xiao, J. Liu, J.-G. Zhang, G. Chen, C. Wang, *Nat. Commun.* **2020**, 11, 3204.
- [15] K. M. Shaju, G. V. Subba Rao, B. V. R. Chowdari, *Electrochim. Acta* **2002**, 48, 145.
- [16] a) J. Choa, M. M. Thackeray, *J. Electrochem. Soc.* **1999**, 146, 3577; b) H. Kim, D.-H. Seo, H. Kim, I. Park, J. Hong, K.-Y. Park, K. Kang, *Chem. Mater.* **2012**, 24, 720.
- [17] M. Dixit, B. Markovsky, F. Schipper, D. Aurbach, D. T. Major, *J. Phys. Chem. C* **2017**, 121, 22628.
- [18] a) J. R. Dahn, E. W. Fuller, M. Obrovac, U. von Sacken, *Solid State Ionics* **1994**, 69, 265; b) Y. Baba, S. Okada, J.-i. Yamaki, *Solid State Ionics* **2002**, 148, 311; c) W.-S. Yoon, K. Y. Chung, M. Balasubramanian, J. Hanson, J. McBreen, X.-Q. Yang, *J. Power Sources* **2006**, 163, 219.
- [19] B. Gillot, J. Baudour, F. Bouree, R. Metz, R. Legros, A. Rousset, *Solid State Ionics* **1992**, 58, 155.
- [20] M. Guilmard, L. Croguennec, D. Denux, C. Delmas, *Chem. Mater.* **2003**, 15, 4476.
- [21] V. Brabers, A. Broemme, *J. Magn. Magn. Mater.* **1992**, 104, 405.
- [22] A. R. Wizansky, P. E. Rauch, F. J. Disalvo, *J. Solid State Chem.* **1989**, 81, 203.
- [23] F. Izumi, K. Momma, *IOP Conf. Ser.: Mater. Sci. Eng.*, **2011**, 18, 022001.